The generation and propagation of the human alpha rhythm

Mila Halgren[a,1,2], István Ulbert[b,c], Hélène Bastuji[d,e], Dániel Fabó[f], Lorand Erőss[c,g], Marc Rey[h,i,j], Orrin Devinsky[k], Werner K. Doyle[k], Rachel Mak-McCully[l], Eric Halgren[m], Lucia Wittner[b], Patrick Chauvel[h,i,j], Gary Heit[n], Emad Eskandar[a,3], Arnold Mandell[o], and Sydney S. Cash[a]

[a]Department of Neurology, Massachusetts General Hospital, Harvard Medical School, Boston, MA 02114; [b]Institute of Cognitive Neuroscience and Psychology, Research Center for Natural Sciences, Hungarian Academy of Sciences, Budapest 1051, Hungary; [c]Faculty of Information Technology and Bionics, Péter Pázmány Catholic University, Budapest 1088, Hungary; [d]Lyon Neuroscience Research Center, Université Claude Bernard, 69100 Villeurbanne, France; [e]Unité d'Hypnologie, Service de Neurologie Fonctionnelle et d'Épileptologie, Hôpital Neurologique, Hospices Civils de Lyon, 69003 Lyon, France; [f]Epilepsy Centrum, National Institute of Clinical Neurosciences, 1145 Budapest, Hungary; [g]Department of Functional Neurosurgery, National Institute of Clinical Neurosciences, 1145 Budapest, Hungary; [h]Division is Institut de Neurosciences des Systèmes, Aix-Marseille Université, 13007 Marseille, France; [i]INSERM, Institut de Neurosciences des Systèmes, 13005 Marseille, France; [j]Assistance Publique–Hôpitaux de Marseille, Timone Hospital, 13005 Marseille, France; [k]Comprehensive Epilepsy Center, New York University School of Medicine, New York, NY 10016; [l]Department of Psychology, University of California, Berkeley, CA 94720; [m]Department of Neurosciences and Radiology, University of California San Diego, La Jolla, CA 93093; [n]Department of Neurosurgery, Permanente Medical Group, Redwood City, CA 94063; and [o]Department of Psychiatry, University of California San Diego, La Jolla, CA 92093

Edited by Gyorgy Buzsáki, New York University Neuroscience Institute, New York, NY, and approved October 11, 2019 (received for review July 30, 2019)

The alpha rhythm is the longest-studied brain oscillation and has been theorized to play a key role in cognition. Still, its physiology is poorly understood. In this study, we used microelectrodes and macroelectrodes in surgical epilepsy patients to measure the intracortical and thalamic generators of the alpha rhythm during quiet wakefulness. We first found that alpha in both visual and somatosensory cortex propagates from higher-order to lower-order areas. In posterior cortex, alpha propagates from higher-order anterosuperior areas toward the occipital pole, whereas alpha in somatosensory cortex propagates from associative regions toward primary cortex. Several analyses suggest that this cortical alpha leads pulvinar alpha, complicating prevailing theories of a thalamic pacemaker. Finally, alpha is dominated by currents and firing in supragranular cortical layers. Together, these results suggest that the alpha rhythm likely reflects short-range supragranular feedback, which propagates from higher- to lower-order cortex and cortex to thalamus. These physiological insights suggest how alpha could mediate feedback throughout the thalamocortical system.

alpha | oscillations | intracranial EEG | laminar | thalamocortical

Alpha oscillations (7 to 13 Hz) (1) are the most salient electroencephalogram (EEG) event during wakefulness and may be fundamental for top-down cognitive processes (2, 3), such as attention (4), perception (5, 6), functional inhibition (7, 8), and working memory (9). However, the underlying neural structure(s) and circuits which generate alpha are intensely controversial. Studies have pointed to the thalamus as the primary alpha pacemaker, with the classic posterior alpha rhythm driven by the pulvinar and/or lateral geniculate nucleus (LGN) (4, 10–12). Within the cortex, it's widely assumed that alpha originates from infragranular layers driven by layer V pyramidal cells (13–17). Despite the prevalence of these hypotheses, the studies used to support them are not definitive; previous electrophysiological literature has either used a distant reference susceptible to volume conduction (4, 13, 15), was performed in vitro (14), or relied on extracranial recordings (18) (*Discussion*). Crucially, none of these hypotheses have been directly tested via invasive recordings in humans. We therefore analyzed focal microelectrode and macroelectrode recordings from human neocortex and thalamus in surgical epilepsy patients to characterize alpha's generation during quiet wakefulness.

Results

We analyzed electrocorticographic (ECoG) recordings of spontaneous alpha oscillations (4.54 ± 0.87 min, mean ± SD) in the occipital, posterior temporal, and posterior parietal cortices of 5 patients (*SI Appendix*, Fig. S1 and Table S1) (ECoG patients [Pts.] E1 to E5; E1, E3, and E4 participated in an eye-closure task, whereas E2 and E5 did not and were recorded during quiet wakefulness). Strikingly, alpha oscillations propagated as traveling waves from anterosuperior cortex toward posteroinferior areas (Figs. 1 and 2 and *SI Appendix*, Figs. S2–S4) (19). To quantify this propagation, we used a 2-pass 3rd-order 0-phase-shift Butterworth filter between 7 and 13 Hz to extract alpha-band activity. The Hilbert transform was then applied to find the analytic signal and, from this, the instantaneous amplitude and phase of ongoing alpha activity; only time points with the highest 20% of alpha-band amplitude (averaged across array channels at each time point) were analyzed further.

To visualize the spatial progression of alpha oscillations across the array, we found the circular difference between the mean phase across all contacts and each individual contact at each point in time (Fig. 1*B*). This yielded a distribution of differences of each contact's phase from the grid's mean phase across all

Significance

The alpha rhythm dominates the electroencephalogram during quiet wakefulness, but the brain structures which generate it are not known. Using rare intracranial recordings in epilepsy patients, we find that alpha rhythms propagate toward the back of the brain and that alpha waves in cortex (particularly superficial layers) lead alpha oscillations in the thalamus. These findings shed light on how the human alpha rhythm coordinates activity throughout the brain.

Author contributions: I.U., E.H., and S.S.C. designed research; I.U., H.B., D.F., L.E., M.R., O.D., W.K.D., R.M.-M., E.H., L.W., P.C., G.H., E.E., and S.S.C. performed research; M.H. and A.M. analyzed data; and M.H. and S.S.C. wrote the paper.

The authors declare no competing interest.

This article is a PNAS Direct Submission.

Data deposition: The data underlying our figures have been made publicly available on figshare, DOI: 10.6084/m9.figshare.9927125.v2. Custom scripts are freely available at https://github.com/mhalgren/AlphaGen. Macaque data are publicly available at http://neurotycho.org/data/20120813ktanesthesiaandsleepchibitoruyanagawa.

[1]To whom correspondence may be addressed. Email: mhalgren@mit.edu.

[2]Present address: Department of Brain & Cognitive Sciences, Massachusetts Institute of Technology, Cambridge, MA 02139.

[3]Present address: Department of Neurological Surgery, Albert Einstein College of Medicine, Bronx, NY 10461.

This article contains supporting information online at https://www.pnas.org/content/pnas/suppl/2019/11/01/1913092116.DCSupplemental/pnas.1913092116.sapp.pdf.

First published November 4, 2019.

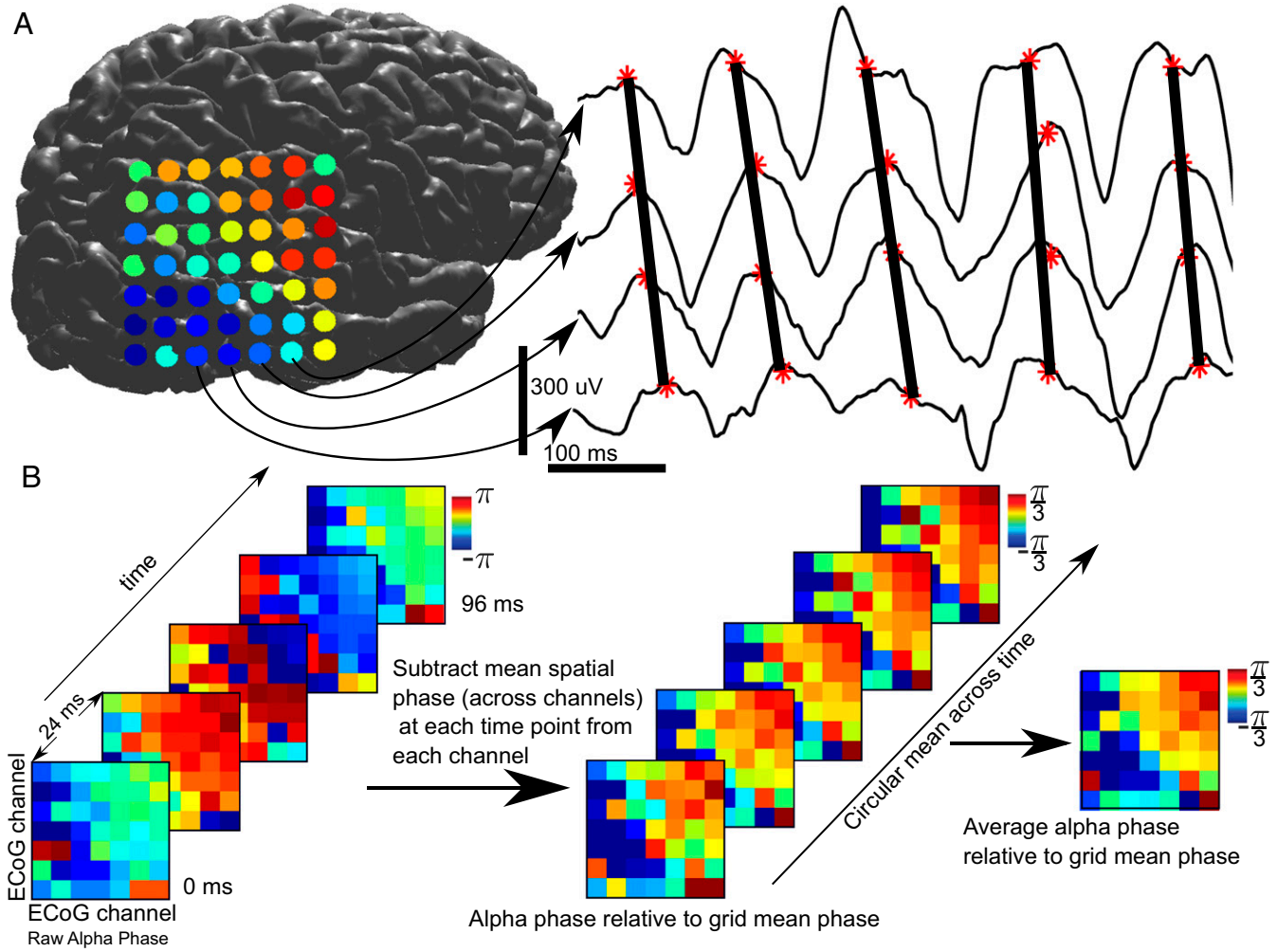

Fig. 1. Analysis stream for ECoG traveling waves. (*A*) Alpha propagates as a traveling wave in the raw broadband data. (*B*) Analysis stream for visualizing traveling waves in ECoG. We start with raw alpha phase of the grid over time. Then, for each time point, we find the circular distance (distance on the unit circle) between each contact and the grid's mean phase (across all contacts) at that time point. Lastly, we find the circular mean of this difference to get each contact's average phase advance or delay.

time points. We then found the circular mean of this difference (across time points): If a contact is leading an oscillation, it will have a positive circular distance with respect to the grid's spatial mean phase; if a contact is lagging, it will have a negative phase difference with the grid's average phase. Fig. 2*B* was then generated by finding the mean circular distance between each contact's phase and the grid's mean phase at each time point, or the average advance/delay of a given contact. This method allows one to measure traveling waves oblique to the grid's implantation and sidestep the selection of a potentially biasing reference contact. However, this analysis only yields a single, average gradient in each patient and makes it hard to assess statistical significance within subjects. We therefore performed a second test to confirm that alpha oscillations had a consistent propagation direction across time in individual patients. This was done by finding the direction of the average spatial phase gradient across the grid of electrodes at each time point, reflecting the average direction of alpha propagation at a single time point, and then determining if the distribution of gradient directions throughout time was nonuniform (20) ($P \leq 10^{-17}$ in each patient, Rayleigh test) (Fig. 2*C*, *Materials and Methods*, and *SI Appendix*, Fig. S4). Estimated median speeds of these waves (derived from the phase gradient) were just under 1 m/s (median speed across patients: 0.9134 ± 0.1563 m/s). (*SI Appendix*, Fig. S4 and *SI Methods*). Open-source ECoG recordings in a healthy macaque during eye closure demonstrated a highly similar propagation direction and speed (21, 22) (Fig. 2*B*).

To determine if the thalamus coordinated these traveling alpha waves, we utilized stereo EEG (SEEG) to make bipolar local-field-potential gradient (LFPg) macroelectrode depth recordings ($n = 9$ patients, 36 ± 7.5 min, mean ± SD) during quiet wakefulness. Recordings were made simultaneously from the cortex and the pulvinar, a thalamic nucleus which projects broadly to posterior cortical regions (23) and postulated to drive cortical alpha (4, 24) (Fig. 3*A*) (SEEG Pts. S1 to S9). The use of a bipolar derivation (i.e., referencing each contact to its neighbor) ensured that activity was locally generated and not volume conducted from a distal structure. Cortical coverage was predominantly posterior (108 of 124 cortical contacts posterior to the central sulcus), similar to our ECoG patients (Fig. 3*B*). We first verified that alpha traveling waves could be measured in these cortical depth recordings by applying the same method used to quantify alpha propagation in our ECoG data (i.e., measuring how much each individual channel's alpha phase led or lagged the mean phase across all channels). Analysis was restricted to occipital and posterior temporal/parietal channels which were in unambiguously lateral cortex; this ensured that the LFPg's polarity was consistent across sites (always surface

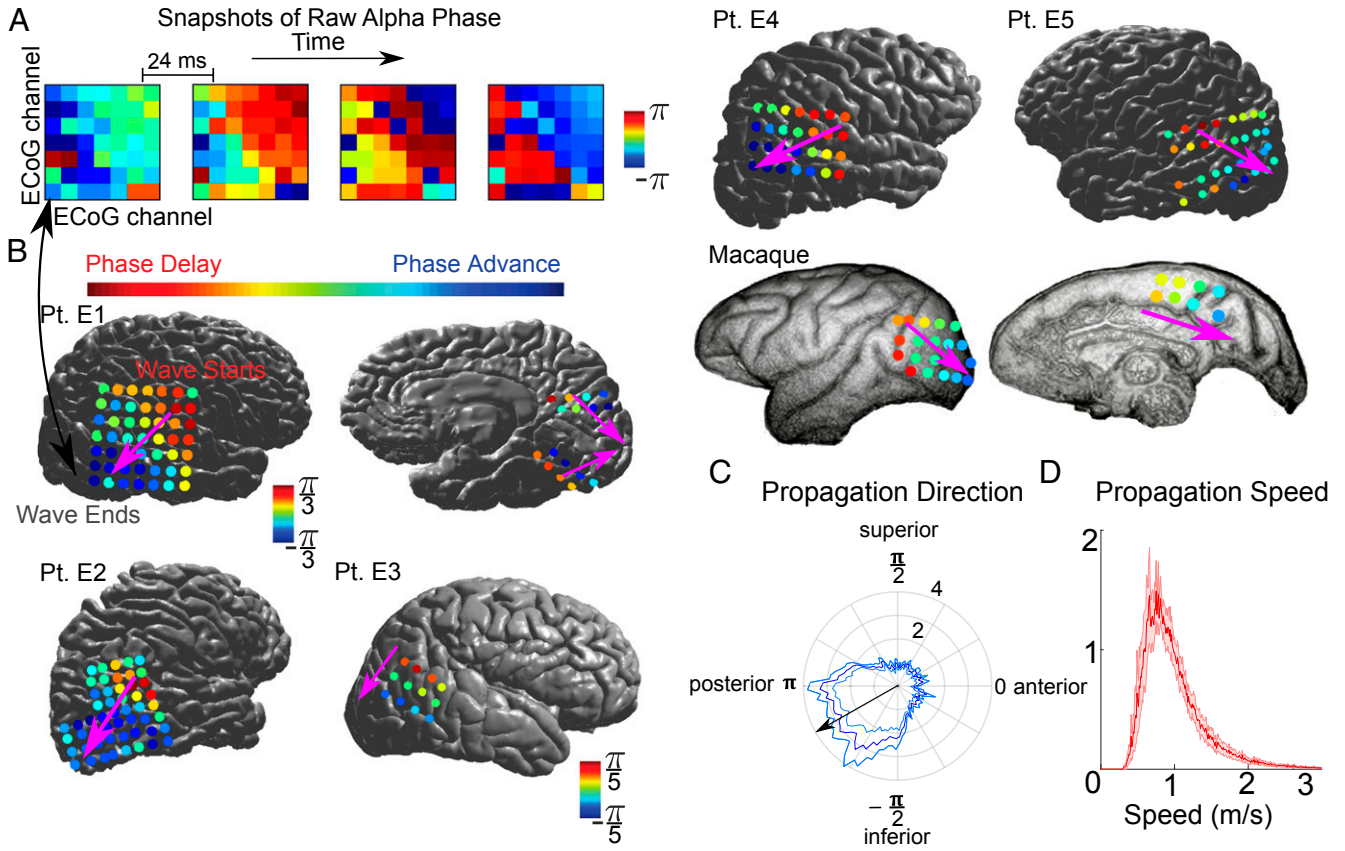

Fig. 2. Alpha propagates from anterosuperior to posteroinferior cortex. (*A*) Alpha-phase snapshots from Pt. L1 demonstrate propagation from the grid's top-right (anterosuperior) to bottom-left corner (posteroinferior). (*B*) Average circular distance of each contact's alpha phase from the spatial mean phase during eye closure. In all patients, alpha propagates toward posteroinferior areas. Overlaid arrow is the direction of the grid's average phase gradient. Color runs from $\pm\frac{\pi}{3}$ in Pts. E1, E2, and E5 and macaque; and from $\pm\frac{\pi}{5}$ in Pts. E3 and E4. (*C*) Average probability distribution of traveling wave directions across time such that the bottom left contact is the most posteroinferior (±SEM across patients). (*D*) Average probability distribution of traveling wave speeds (±SEM across patients).

positive, given that we subtracted medial from lateral contacts for each bipolar pair). Just as with our ECoG recordings, we only analyzed time points with the top 20% of cortical alpha power (averaged across channels at each time point). The alpha phase of anterosuperior contacts led ones closer to the occipital pole, replicating our ECoG recordings (Fig. 4*A* and *SI Appendix*, Fig. S6). This demonstrates that these traveling waves are not reference-dependent and suggests that the alpha rhythms recorded in our depth patients are analogous to the ones recorded in our ECoG patients. As we then wished to examine the pulvinar's role in cortical alpha, all further analyses were biased toward thalamic activity by only analyzing the 2-s epochs with the 20% most thalamic alpha-band power (averaged across all thalamic channels). First, we characterized the prevalence of alpha rhythms in both cortex and pulvinar. This was done by detecting which channels had peaks between 7 and 13 Hz in their power spectra (peaks were detected via the peakfinder algorithm; *Materials and Methods*). Surprisingly, power spectra from cortical contacts had alpha-band peaks more frequently (63.4%; 78 of 123 of cortical channels) than ones in the pulvinar (34.6%; 9 of 26 of thalamic channels) (Fig. 4*B*, *Materials and Methods*, and *SI Appendix*, Fig. S7) Thalamic and cortical power spectra also sometimes had different peak frequencies (Fig. 4*B*); while this could be construed as evidence for separate thalamic and cortical alpha generators, this is not necessarily the case. Empirically, spindles (believed to be thalamocortically driven) have higher frequencies in the thalamus than the cortex (25). Analytically, weakly coupled oscillators can also exhibit different peak frequencies, despite driving one another (26). Thalamocortical coherence spectra often exhibited robust alpha peaks (Fig. 4*E*), indicating that alpha rhythms in the posterior cortex and pulvinar are functionally coupled (peak alpha coherence in thalamocortical channel pairs with significant alpha coherence: 0.3346 ± 0.012, mean ± SEM). As a first means of determining whether neocortical alpha led thalamic alpha (or vice versa), we detected alpha bursts in both thalamic and cortical channels. Briefly, a putative burst was detected when alpha-band power (7 to 13 Hz, hilbert.m) exceeded 3 times the average of theta-band (4 to 6 Hz) and beta-band (15 to 25 Hz) power. Burst starts and stops were defined as when alpha-band power was at least 2 times the theta/beta average, and all bursts less than 400 ms were then rejected. Lastly, alpha bursts which were less than 50 ms apart were merged. For each thalamocortical channel pair, we determined if cortical bursts started significantly before thalamic bursts (or vice versa). By the binomial test, 28 of 362 thalamocortical channel pairs ($P < 0.05$, Bonferroni corrected across all 362 channel pairs) had a significant lead in alpha onset. In all 28 of these channel pairs, cortical alpha bursts led thalamic alpha bursts (Fig. 4*C* and *SI Appendix*, Fig. S8). Importantly, a previous study applying a similar burst-detection algorithm to analyze sleep spindles in the same subjects and channels during sleep found the opposite directionality—i.e., that thalamic spindles led cortical spindles (25). As a second measure of cortical alpha leading thalamic alpha power, we measured the cross-covariance of alpha amplitude (as derived from the amplitude envelope of the analytic signal) in thalamocortical channel pairs with statistically significant alpha

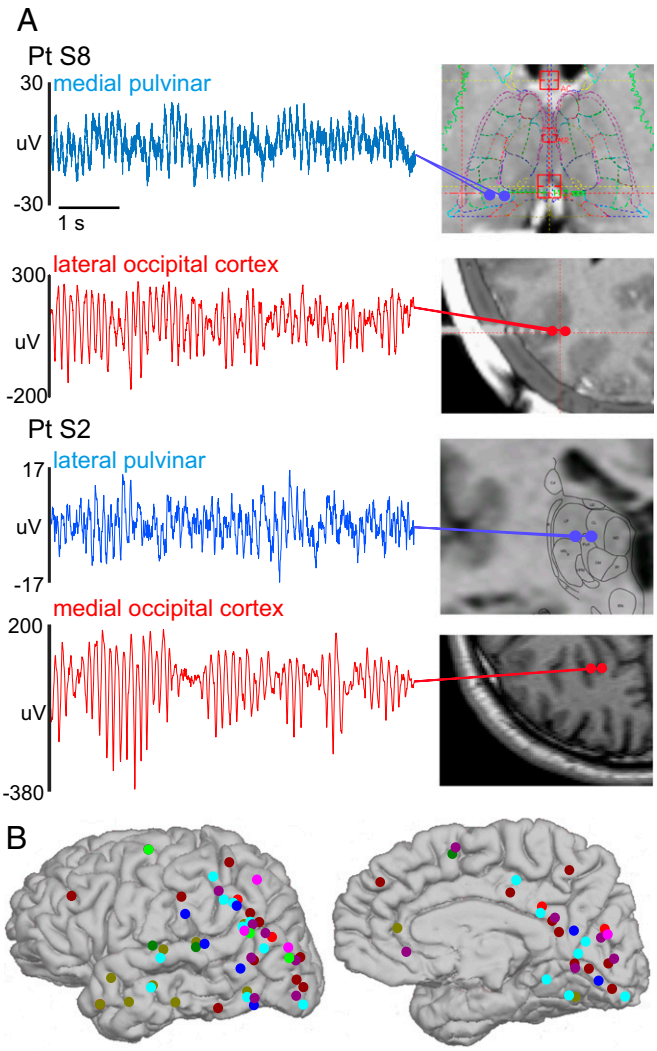

Fig. 3. Robust alpha rhythms can be recorded in human pulvinar and cortex. (*A*) Representative 6-s LFPg traces of simultaneous thalamic and cortical alpha activity. Prominent, largely continuous alpha rhythms can be recorded in various locations within the pulvinar as well as posterior cortex. (*B*) Cortical implant locations in all SEEG patients displayed on Pt. S3's brain. Each color signifies a different patient.

coherence (189 of 362) (27). This analysis was largely equivocal, but weakly favored cortical leading thalamic alpha (*SI Appendix*, Fig. S9 and *SI Methods*).

To further determine whether cortical or thalamic activity was driving these rhythms, we extracted high gamma power (HGP), a rough proxy for neural firing, in both structures ($n = 5$; 70 to 120 Hz in Pts. S1 to S3 due to a low sampling rate, 70–190 Hz in Pts. S8 and S9; Pts. S4 to S7 were excluded due to low sampling rates; note that using the same 70- to 120-Hz HGP band in Pts. S8 and S9 didn't substantially change the results; *Materials and Methods*). If a given structure is generating alpha oscillations (and if local HGP reflects neural firing), its HGP should be synchronous with its alpha-band LFPg and exhibit phase-amplitude coupling (PAC) (28). PAC was assessed by using 2 methods: Tort's Modulation Index (MI) (29) and the coherence between the time-domain LFPg and HGP (30) (Fig. 4*E* and *SI Appendix*, Fig. S10 and *SI Methods*). To ensure that this PAC wasn't spuriously driven by sharp waveforms (31), we measured the sharpness ratio (SR; *SI Appendix*, *SI Methods*) of each channel's alpha and then measured the correlation of this with the strength of each channel's PAC quantified by its MI. SR and MI were not significantly correlated, trending toward anticorrelation (i.e., smoother waveforms had more PAC), the opposite of what would be expected if our PAC was spurious ($r = -0.2124$, $P = 0.0602$) (31, 32). Notably, thalamic alpha was rarely coherent with its own HGP (coherence: 0 of 14 intrathalamic contact pairs, MI: 3 of 14, $P < 0.05$, Bonferroni corrected within patients); instead, thalamic alpha rhythms were predominantly synchronous with cortical HGP (coherence: 9 of 14, MI: 10 of 14; mean peak alpha coherence between thalamic LFPg and cortical HGP channel pairs with significant coherence of 0.3535 ± 0.026) (Fig. 4 *D* and *E*), supporting cortical generation.

Because HGP is an imperfect proxy for neuronal firing (33), the failure to find consistent local thalamic PAC could reflect a limitation of our recordings rather than a cortical origin for alpha [but it should be noted that thalamic HGP is modulated by thalamic sleep spindles in the same recordings (25)]. To resolve this ambiguity, we further analyzed the minority of thalamic channels (5 of 42 intrathalamic contact pairs) in which alpha LFPg was phasic with HGP in at least 1 thalamic and cortical channel. These channel pairs gave us the opportunity to examine average HGP in both the thalamus and cortex at different thalamic alpha phases. Unlike the relative LFPg phase, which is uninterpretable in the thalamus due to its nonlaminar structure, differences in mean HGP with respect to the alpha LFPg phase can be interpreted as lags of putative population spiking activity (25). By averaging the mean cortical and thalamic HGP with respect to the phase of thalamic alpha LFPg phases across channel pairs, it is apparent that cortical HGP leads thalamic HGP (Fig. 4*F*). In individual thalamocortical channel pairs, this could be quantified by measuring the cross-covariance between the thalamic and cortical HGP profiles and seeing if the peak was positive/negative or examining which had minimal HGP at an earlier thalamic alpha phase. Cortex led thalamus in all 5 channel pairs, as derived by both measures, more than expected by chance ($P = 0.0313$, 1-tailed binomial test of cortex leading thalamus against thalamus leading cortex). This lag (difference between HGP minima, as seen in Fig. 4*F*) was on average ~40°, or ~11 ms, assuming an alpha period of 100 ms. This time delay is physiologically plausible and similar to how much the thalamus leads cortex during sleep spindles (25).

As a final directional measure, we measured the Granger causality (GC) spectrum (which quantifies the amount of information one time series contains about another across frequencies) of the LFPg between all pairs of cortical and thalamic contacts (34) (Fig. 4*G*). Corticothalamic causality in the alpha band was found to be significantly greater than thalamocortical causation for almost every thalamocortical channel pair (across all patients), with a significant difference between thalamocortical and corticothalamic causation ($P \leq 0.01$ for each channel pair, Wilcoxon signed rank test, Bonferroni corrected within patients; 143 of 163 [87.73%] pairs with greater corticothalamic than thalamocortical causality; $P < 1.83 \times 10^{-24}$ across all significantly different channel pairs, binomial test). To ensure that this wasn't due to our cortical channels having greater alpha power, we repeated our Granger analysis only using thalamocortical channel pairs in which the thalamic lead had greater normalized alpha power. This actually increased the percentage of channel pairs with significantly greater corticothalamic than thalamocortical alpha causality (74 of 82 [90.24%], significantly more than chance as determined by the binomial test, $P < 7.2 \times 10^{-15}$).

To determine which cortical layers generate the alpha rhythm, we utilized laminar microelectrodes (35) in the occipital, temporal, and parietal cortex to record current-source density (CSD; $n = 3$), HGP, and multiunit activity (MUA) ($n = 2$) across gray-matter layers during quiet wakefulness (11.32 ± 0.48 min, mean ± SD) (35) (Fig. 5) (laminar Pts. L1 to L3). The CSD is the second spatial derivative of the monopolar field potential, which yields a volume-conduction-free measure of local transmembrane

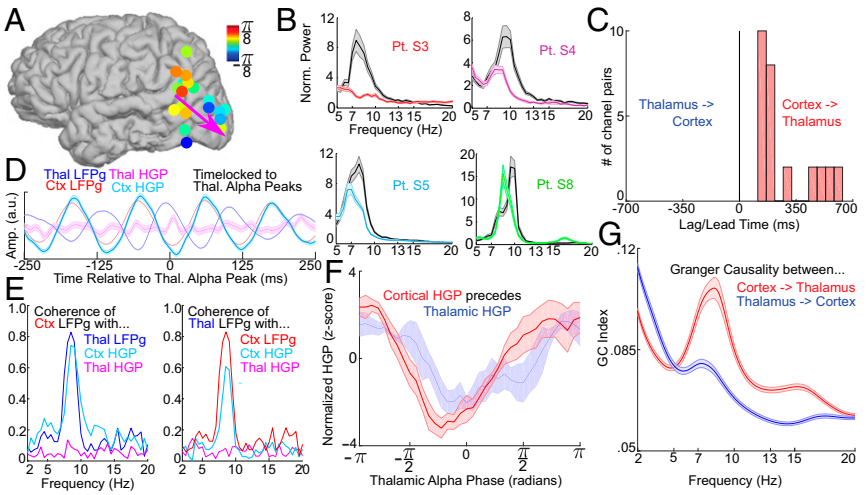

Fig. 4. Cortical alpha leads thalamic (pulvinar) alpha. (*A*) Average alpha-phase lag/leads in bipolar contacts ($n = 5$). Note that anterosuperior channels lead inferoposterior ones, in accord with our ECoG recordings. (*B*) Power spectra of the thalamic (color) and cortical (gray) channel with the greatest alpha power. (*C*) The difference in start times between all cortical and thalamic alpha bursts (start time in thalamus to start time in cortex) in the 28 channel pairs with a significant thalamic or cortical lead ($P < 0.05$, Bonferroni corrected, binomial test). Alpha bursts start (on average) in cortex for all 28 channel pairs. (*D*) Cortical and thalamic LFPg and HGP from representative channels locked to peaks in thalamic alpha LFPg—cortical, but not thalamic, HGP is phasic with thalamic LFPg. (*E*) Coherence spectra of thalamic and cortical LFPg with thalamic and cortical HGP and LFPg from the same channel pair in *D*; the coherence of thalamic LFPg with cortical HGP (but not thalamic HGP) suggests that the cortex may drive thalamic alpha activity. (*F*) Normalized thalamic and cortical HGP at different thalamic alpha phases averaged across channels; note that cortical HGP slightly leads thalamic HGP. (*G*) GC spectra averaged over all thalamocortical contact pairs; corticothalamic causality shows a strong alpha peak. Amp., amplitude; a.u., arbitrary units; ctx, cortical; norm., normalized; thal, thalamic.

currents surrounding the laminar probe (35, 36). MUA [filtered online at 200 to 5,000 Hz, then filtered offline at 300 to 3,000 Hz and rectified (35)] and HGP (filtered offline at 70 to 190 Hz) are also spatially focal and reflect neural firing (37). By quantifying both transmembrane currents [which generally reflect postsynaptic events (38)] and firing within each cortical layer, we can determine which laminae generate the alpha currents and firing measured extracortically with ECoG, magnetoencephalography, and EEG (36, 39–41). Similar to our previous analyses, we only utilized artifact-free 2-s epochs with the 20% most alpha-band power. Despite being recorded from various regions of cortex, alpha-band currents in all patients were strongest within superficial cortical

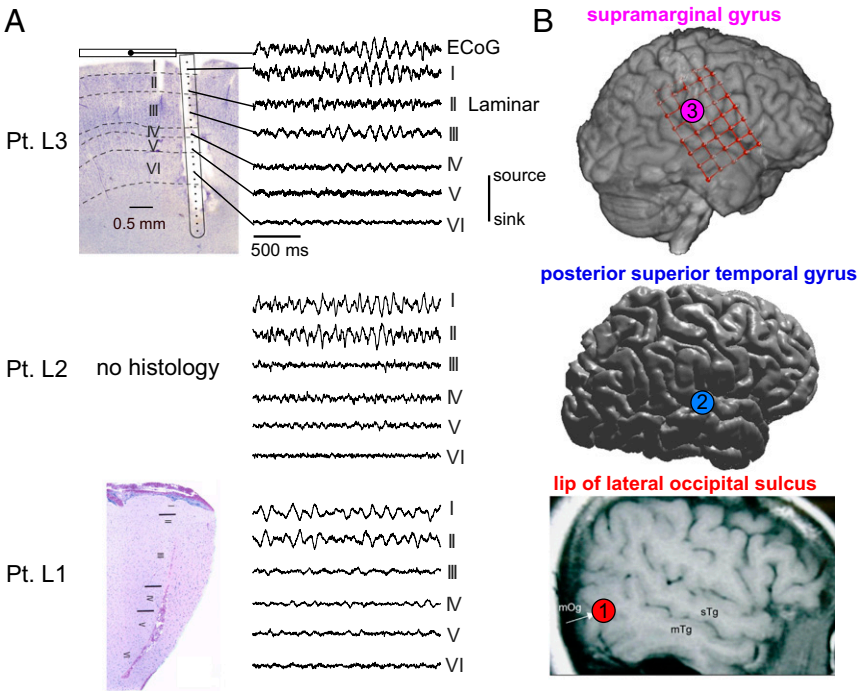

Fig. 5. Laminar recordings of cortical alpha. (*A*) Nissl stains of the explanted tissue surrounding the laminar probe in Pts. L1 and L3, in addition to representative laminar CSD traces from each layer in each subject. Note that despite being made in distinct cortical locations, alpha oscillations were always strongest in layer I/II. Furthermore, in L3, the trace of a simultaneously recorded overlying ECoG contact is near identical to the underlying laminar layer I. (*B*) Locations of each laminar probe in all patients. Adapted with permission from ref. 86.

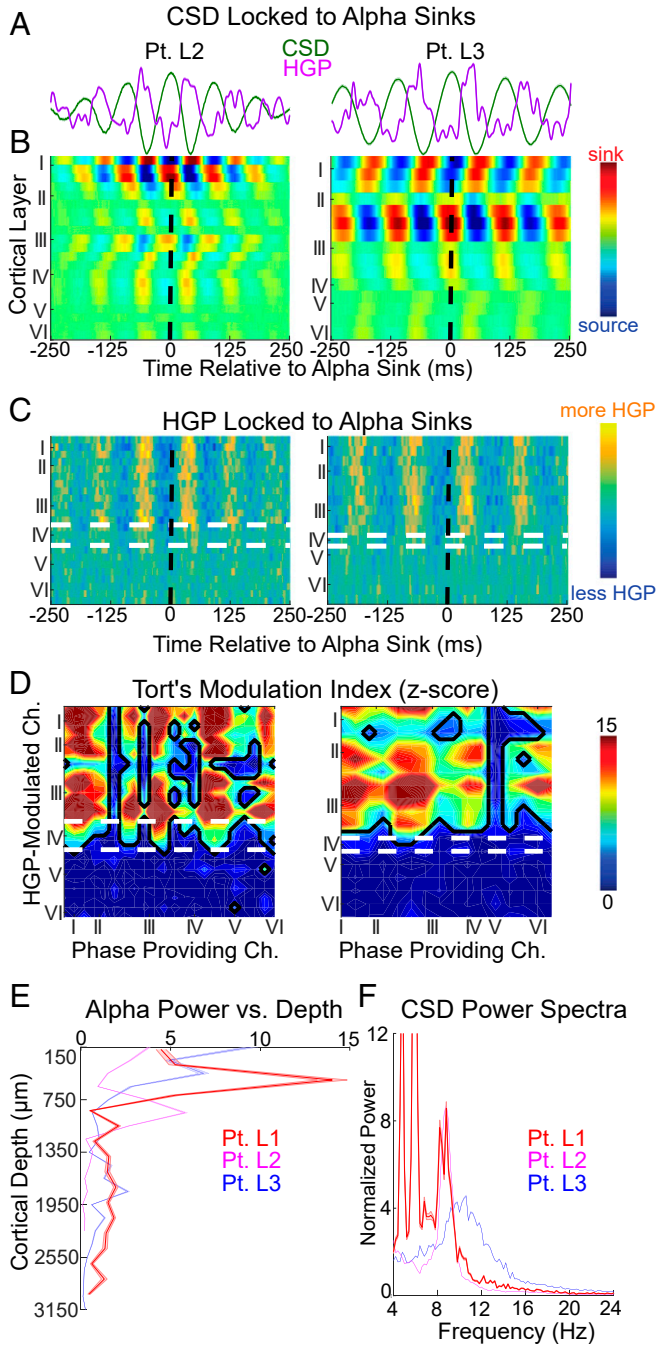

Fig. 6. Alpha CSD and HGP are maximal in supragranular cortex. (*A*) Average CSD and HGP waveforms of a single channel on the same time axes as *B* (±SEM across alpha sinks). (*B* and *C*) CSD (*B*) and HGP (*C*) averaged on current sinks in channels 3 and 6 in Pts. L2 and L3, respectively; white and black dashed lines indicate layer IV boundaries and the time of the alpha sink, respectively. (*D*) Z score of the MI between alpha phase and HGP across all channels (Ch.). (*E*) Average alpha power throughout the cortical depth (±SEM across epochs). (*F*) Power spectra of the channel with greatest alpha power in each subject (±SEM across epochs).

layers (Pt. L1: $P < 2.27 \times 10^{-25}$; Pt. L2: $P < 1.9 \times 10^{-22}$; Pt. L3: $P < 1.66 \times 10^{-5}$; largest P values of Wilcoxon sign rank comparing mean alpha power in supragranular versus granular and infragranular channels across epochs, Bonferroni corrected) (Figs. 5 and 6 *B* and *E* and *SI Appendix*, Fig. S11).

Averaging HGP on alpha current sinks as well as measuring Tort's MI between alpha CSD and HGP (Fig. 6 *B–D*) suggested that alpha-band firing is located in layers I through III. Interestingly, while HGP was modulated by alpha throughout layers I through III, significant MUA modulation was restricted to layer III (Fig. 7). It's not clear whether this reflects differential sensitivity to noise or suggests that MUA and HGP have divergent neural generators. In accord with the latter hypothesis, recent laminar recordings found that HGP was driven by dendritic processes as well as spiking, consistent with our HGP modulation being superficial to MUA (the latter reflecting firing at the soma) (42). Despite this difference, the MUA and HGP profiles averaged across all laminar channels and triggered on alpha troughs were highly similar (Pt. L2: $r = 0.6756$, $P = 0$; Pt. L3: $r = 0.4493$, $P = 0$), and both measures imply that the firing of supragranular (and not infragranular) pyramidal cells are phasic with the human alpha rhythm. Furthermore, this supragranular firing was maximal during very superficial sinks and minimal during superficial sources, consistent with active synaptic and/or voltage-gated currents in layers I/II. The sink-over-source current dipole associated with increased firing would be recorded with ECoG/(M)EEG as surface-negative, as the negative end of the dipole (a sink of current flowing away from the extracellular space) is closer to the surface electrode. Consequently, this sink–source configuration comports with previous studies (39, 43) reporting that firing is maximal during the surface-negative trough of the alpha rhythm and maximal during its surface-positive peak.

Lastly, we tested if the traveling alpha waves recorded with ECoG corresponded to the supragranular alpha oscillations recorded with laminar probes. To demonstrate this, we made combined ECoG-laminar recordings in Pt. L3 to record the same alpha rhythm at both local (laminar) and global (ECoG) scales (44) (Fig. 8). Robust alpha oscillations [likely the classical mu rhythm given the electrodes' locations (45)] were measured with ECoG from perirolandic cortex and with a simultaneously implanted laminar probe from the supramarginal gyrus; both recordings exhibited nearly identical alpha peaks (Fig. 8*E*), and averaging the laminar CSD on ECoG alpha troughs revealed strong supragranular sinks and sources (Fig. 8*F*). Alpha propagated as a traveling wave throughout the grid (Fig. 8 *A–D*) with a similar median speed (0.62 m/s) to traveling waves in posterior cortex. If the supragranular alpha measured with laminar probes

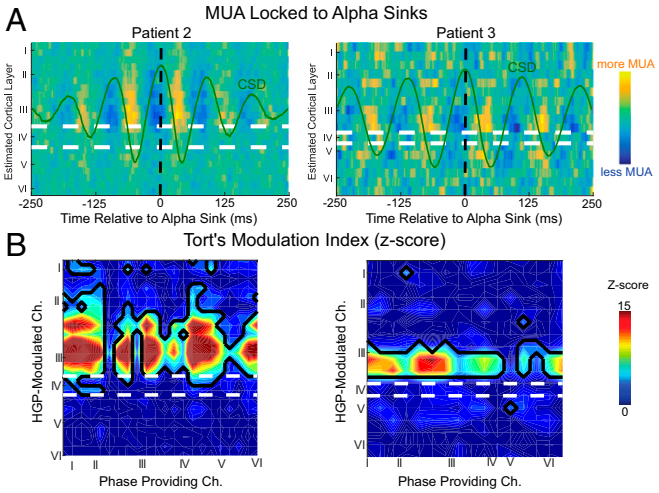

Fig. 7. MUA is modulated in layer III. (*A*) MUA averaged on current sinks on the channels with the greatest alpha power (channels 3 and 6, respectively), which is most clearly modulated within lower layer III. (*B*) Tort's MI between alpha CSD phase and MUA amplitude over all laminar contact pairs—note that firing is correlated with alpha phase in both superficial and deep cortex. Ch., channel.

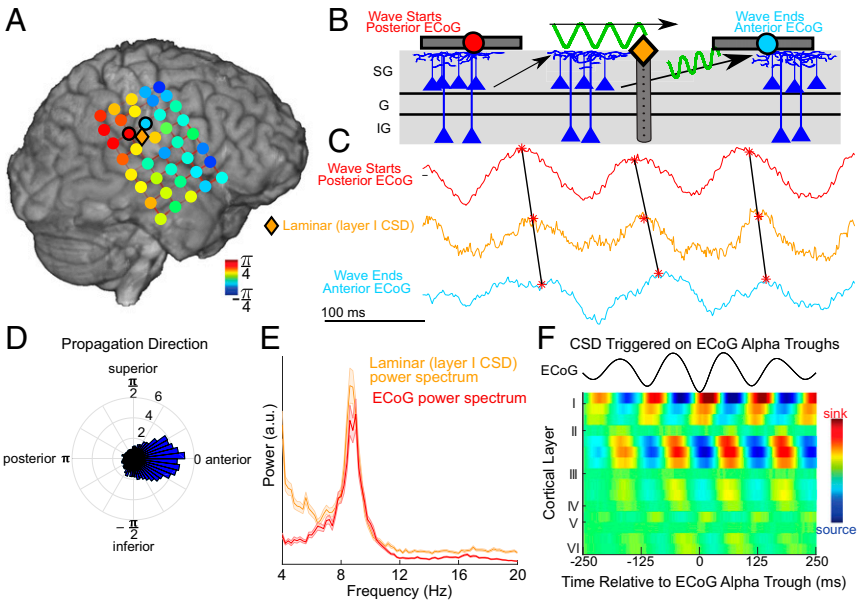

Fig. 8. Simultaneous ECoG–laminar recordings reveal traveling alpha waves which propagate through supragranular cortex. (*A*) Average circular distance of each ECoG (circles) and layer I laminar (diamond) contact's alpha phase from the spatial mean phase throughout the ECoG grid. Note that the laminar's alpha phase is intermediate to neighboring ECoG contacts, suggesting that ECoG and the laminar probe recording the same traveling wave at different scales. (*B*) Representative drawing of a traveling alpha wave (as measured with ECoG) propagating through superficial layers (as measured by a laminar probe). (*C*) Example traces from ECoG contacts posterior (red) and anterior (blue) to the laminar probe. Alpha phase in the laminar is intermediary to the ECoG contacts. (*D*) Distribution of traveling wave directions; mu waves propagate from posterior (higher-order) toward anterior (lower-order) cortex. (*E*) Power spectra from simultaneous laminar and ECoG recordings; they share a near-identical alpha peak. (*F*) Laminar CSD averaged on troughs in the nearest ECoG contact. Note that alpha activity is superficial.

underlies the traveling alpha waves recorded with ECoG, we should be able to observe traveling alpha waves propagating through the supragranular layers of the laminar probe with a phase between its neighboring ECoG contacts (Fig. 8*C*). To establish this, we measured the average phase advance/delay of the CSD in the laminar's most superficial channel with respect to the grid's mean phase and found a phase lag intermediate to that of neighboring ECoG contacts (Fig. 8*A*; this was also demonstrated by measuring the phase of the coherence between laminar and ECoG in *SI Appendix*, Fig. S13).

Interestingly, the direction of propagation was posterior to anterior (Fig. 8*D*). While this may appear to conflict with our recordings of posterior alpha (which propagated anterior to posterior toward the occipital pole), the reversed propagation direction is consistent with alpha propagating from higher- to lower-order cortex in both systems, as associative (higher-order) somatosensory areas are posterior to primary somatosensory cortex (46–48). Future studies should record somatosensory alpha from more patients to confirm that this effect is robust.

Discussion

Our results suggest that alpha contributes to feedback processing within and across brain regions and structures (Fig. 9). The anatomical propagation of posterior alpha traveling waves from anterosuperior to posteroinferior cortex implies a functional progression from higher-order to lower-order visual areas, matching

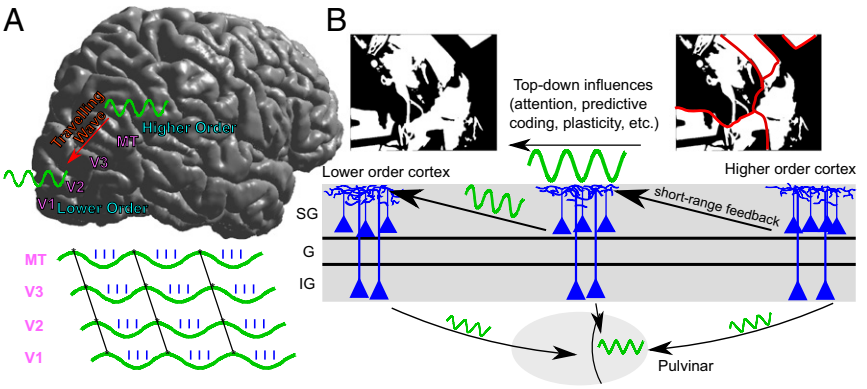

Fig. 9. Tentative model for how alpha's physiology could mediate feedback. (*A*) Alpha propagates as a traveling wave from higher-order (middle temporal, visual area 3) toward lower-order visual areas 1/2 cortical areas. (*B*) Alpha is strongest within supragranular cortex and may carry top-down information via short-range feedback connections to constrain lower-level processing; for instance, alpha may play a role in resolving ambiguous visual imagery, such as the picture of a woman and a horse's snout shown above. Cortical alpha in layer VI might influence alpha activity within the pulvinar. Reproduced with permission from ref. 87, which is licensed under CC BY 4.0.

alpha's putative role as a feedback rhythm (13). Alpha also propagated from associative (posterior) to primary (anterior) areas within somatosensory cortex, leading to a reversed physical propagation direction but the same hierarchical one. Interestingly, previous scalp studies of human traveling alpha waves have also found varying propagation directions (2, 49), in contrast to the consistent anterior–posterior directionality we observed. This may be due to scalp recordings of alpha reflecting a volume-conducted mixture of traveling alpha waves with different directions traversing distinct cortical hierarchies, consonant with our demonstration of posterior-to-anterior alpha propagation in somatosensory cortex. Alternatively, propagation direction might change with task or behavioral state (49, 50); our macaque analysis provided some evidence for this, as eye opening induced a clear (though much smaller) peak of directional propagation from posterior to anterior areas (*SI Appendix*, Fig. S4). Recent studies which used ECoG to study alpha traveling waves also appeared to find that alpha within posterior cortex generally propagates toward the occipital pole, although they do not explicitly draw this conclusion (43, 51). That their propagation directions were less consistent could be due to differences in state, as much of our data were collected during eye closure (which greatly increases alpha power), whereas theirs was collected during tasks. Alpha traveling waves might serve as a mechanism to internally scan the attentional field, tag distinct visual features with different phases (52), or facilitate plasticity between upstream and downstream areas (53, 54).

Simultaneous recordings from human cortex and pulvinar provided several measures suggesting that cortical alpha leads thalamic alpha during quiet wakefulness. Thalamic alpha was less common than cortical alpha, and discrete alpha bursts in cortex led alpha bursts in the thalamus. Furthermore, thalamic alpha LFPg was synchronous with cortical HGP (putative firing) more often than thalamic HGP; when thalamic alpha was synchronous with both cortical and thalamic HGP, HGP in the cortex led HGP in the thalamus. However, because HGP is an imperfect proxy for spiking (33, 42), this finding must be confirmed with single unit recordings in animal models. Finally, thalamic alpha was Granger caused by cortical alpha.

A potential weakness of these bivariate causal analyses is the possibility of a third structure (not recorded from) driving alpha oscillations in both pulvinar and posterior cortex, such as the LGN (10). While this is a possibility, the LGN is an unlikely cortical pacemaker, as its major projections are limited to striate and circumstriate cortex (23), and we found that alpha oscillations propagate toward (and not from) the occipital pole. Because the LGN and pulvinar are the 2 thalamic nuclei with the most robust projections to posterior cortex capable of driving visual alpha, these findings agree with strong cortical influences on thalamic (pulvinar) alpha during quiet wakefulness (though this conclusion only follows for posterior/visual alpha). While this appears to contradict animal studies in which the pulvinar drove cortical alpha (4), it's consonant with findings that the cortex can still generate alpha in vitro (14) and actually shows increased alpha-band power when the pulvinar is inactivated (24), as well as alpha coherence within the cortex exceeding thalamocortical alpha coherence (55). These findings can be reconciled with other studies supporting thalamic alpha generators (4, 56) in a number of ways. There may be separable thalamic and cortical alpha pacemakers which become differentially active and coupled under different behavioral conditions (4, 57)—for instance, this effect may be dependent on eye closure, which was not controlled for in these recordings. Alternatively, the oscillatory circuit required to generate alpha may require both thalamic and cortical cells, or the pulvinar could enable an intracortical alpha pacemaker with tonic (nonrhythmic) excitation/inhibition without being a direct pacemaker (58), perhaps coordinating cortical alpha phase in a task-relevant fashion (4). Diffuse thalamocortical matrix projections might mediate this, as matrix projections target superficial cortical layers (59) (in which we found alpha power to be strongest). Nuclei besides pulvinar or LGN, and particularly those with diffuse projections such as the medial dorsal or ventromedial nuclei, could also be involved in generating visual cortical alpha (60). Though direct measurements and causal manipulation of spiking activity in animal models are needed to prove this, the simplest explanation for our findings is a leading role for the cortex driving alpha in the pulvinar during quiet wakefulness. Functionally, corticothalamic alpha might inhibit the thalamus to gate feed-forward processing and suppress irrelevant neural assemblies akin to its putative role within the cortex (7), as low-frequency corticothalamic activity can inhibit thalamic firing (61).

Laminar microelectrode recordings demonstrate that alpha oscillations reflect layer I/II currents [postsynaptic (38)] and layer I through III firing (presynaptic), demonstrating that supragranular layers are the source of alpha LFPs and HGP recorded via ECoG and (M)EEG. However, inferring the neural circuit mechanisms which generate the alpha rhythm from our laminar recordings is more complex. As supragranular pyramidal cells (which is where we observed alpha-phasic firing) are known to make feedback projections to layers I/II (where we recorded driving currents), our recordings support layer II/III pyramidal cells as the primary alpha generators within the cortex during quiet wakefulness. Our ECoG recordings also support this, as the short-range feedback projections subserved by supragranular pyramidal cells (62) are a likely intracortical mechanism for mediating the continuously propagating top-down traveling waves measured by using ECoG. These projections would enable oscillations which propagate continuously from high- to low-order cortex (i.e., not in the saltatory manner that might be expected if mediated by long-range feedback) at <1 m/s [the conduction velocity of intracortical fibers (63)] (Fig. 9). While most models posit that layer V (infragranular) pyramidal cells drive alpha within the cortex (13, 14), these are based mostly on monopolar LFP recordings (39, 64), which (unlike CSD) are prone to volume conduction from deep sources. Some studies in macaque cortex appear to circumvent this by reporting significant alpha-band CSD-MUA coupling in deep layers of V1, V2, and V4 (41). However, it should be noted that these studies did not report CSD alpha power across the cortical depth [unlike another study which found that supragranular cortex had the most alpha power in each macaque primary sensory area (39)], and prior to calculating their directional measures, they aligned their data to peaks/troughs in the channel with the most monopolar LFP alpha power. As this channel was likely infragranular [volume conduction leads to monopolar alpha power being spuriously maximal in deeper cortex (39)], this may have biased their results toward granular/infragranular generators. Importantly, CSD alpha power being greatest in superficial layers is consistent with alpha-reflecting currents on the apical dendrites of supragranular or infragranular pyramidal cells; our paper resolves this ambiguity by measuring the coherence between alpha currents and MUA throughout the cortical depth and finding significant modulation of only supragranular firing by alpha currents [though a study in macaques did report modulation of granular MUA by superficial alpha CSD (39)]. Further work employing causal manipulation of infragranular cortex in animal models, as well as controlling for behavioral state and eye closure, will be needed to determine the role of deeper layers in alpha generation. How does this compare to the cortical generation of other rhythms? Slow waves, delta and theta in humans, are also strongest in superficial layers (65–67); this may indicate that, in humans, supragranular cortex plays a privileged role in sustaining low-frequency oscillatory activity. Laminar recordings made in homologous areas and states across species will be necessary to determine if this is unique to humans, extends to primates, or is true across species. An important limitation of our study is that only 1 of our laminar

recordings was made from occipital cortex (and therefore reflected the classical posterior alpha rhythm). Despite this, all 3 laminar recordings showed a very similar profile of alpha currents and HGP/MUA (Figs. 5 and 7 and *SI Appendix*, Fig. S11). Though there are different sensory alphas in the cortex, our work complements other findings which find broadly similar alpha physiology across areas (39, 68, 69). However, careful work will need to be done to tease apart how alpha varies between regions. In all, our microelectrode recordings strongly suggest that cortical alpha reflects short-range intracortical feedback mediated by supragranular pyramidal cells within superficial layers.

This supports an integrative function for alpha, due to the termination of widespread associative connections in superficial layers (62) and the modulatory role of layer I/II apical dendrites (66, 70). A supragranular origin for the alpha rhythm is also in accord with its putative role in neural inhibition (68), as layers I/II contain a dense interneuronal network which strongly inhibits the apical dendrites of excitatory cells throughout the cortical column (71). This short-range inhibition would allow higher-order cortex to modulate the gain of lower-order areas throughout visual cortex, providing a laminar circuit for top-down processes such as attention. Further studies which combine cognitive tasks with invasive recordings are needed to understand the implications of our findings for alpha's behavioral role, as the physiology we describe is consistent with a breadth of potential functions for alpha. In all, we find that alpha acts within the nervous system by propagating from cortex to thalamus and higher-order to lower-order cortex, likely via short-range supragranular feedback projections. These intracortical and corticothalamic dynamics could allow alpha to sculpt activity throughout the neural hierarchy.

Materials and Methods

Patients. Implantations were performed on patients with pharmacologically resistant epilepsy undergoing surgery to locate and resect seizure foci. Laminar and ECoG recordings were made from hospitals in the United States and Hungary, and thalamocortical depth recordings were performed in France (*SI Appendix*, Table S1). Seventeen patients (10 female, ages 15 to 50) were informed of potential risks and told that they had no obligation to participate in the study, as well as being informed that their decision to participate wouldn't affect their clinical care. Experiments were made with fully informed consent as specified by the Declaration of Helsinki and were approved by local institutional review boards (IRBs). These boards included the Partners Health Care IRB, the New York University Medical Center IRB, the Stanford University IRB, the RIKEN Ethics Committee, and the Hungarian Medical Scientific Council. All decisions concerning macroelectrode placement were made solely on a clinical basis, whereas laminar microelectrodes were inserted into cortex likely to be resected.

Patients were numbered according to their modality (E# for ECoG, S# for SEEG/macroelectrode depth, and L# for laminars). Numbering for patients was started anew for each measurement modality, and no patients had more than 1 kind of electrode (ECoG, SEEG, or laminar) analyzed with the exception of L3 (no corresponding ECoG number).

All recordings other than those during our eye-closure task were made of spontaneous activity during quiet wakefulness, in which the patient was not engaged in a cognitive task.

General Analysis Procedures. Recordings were analyzed by using custom MATLAB scripts with the CircStat (72) and Fieldtrip (73) Toolboxes.

Prior to further analysis, the raw data were visually inspected for artifacts due to machine noise, patient movement, or epileptiform activity. Epochs containing these artifacts (as judged by an expert neurologist) were removed prior to further analysis.

Unless otherwise specified, all analyses of alpha-band effects refer to the 7- to 13-Hz band. Error bars correspond to the SEM.

Power and cross-spectral densities were found via the multitaper method. This was performed by applying a Hanning taper and then taking the Fourier transform of the zero-meaned data.

Coherence (Fig. 4*E* and *SI Appendix*, Figs. S10*A* and S13) was calculated by using the ft_connectivity function, which defines the coherence between mean subtracted time series x and y as $Coh(x,y) = \left|\frac{S_{xy}}{S_{xx}S_{yy}}\right|$, where S_{xy} is the cross-spectral density between x and y and S_{xx} is the autospectral density of x (74) (*SI Appendix, SI Methods*).

To derive alpha and high-gamma amplitude as well as alpha phase, we used the Hilbert transform. First, data were filtered by using a 2-pass 4th-order IIR Butterworth filter. Then, the analytic signal $z(t)$ was found by applying the Hilbert transform to the filtered signal of each channel. The phase series $\varphi(t)$ was found by taking the angle of the analytic signal, and the amplitude $A(t)$ of every channel was found by taking the real component of the analytic signal.

As a second measure of the alpha rhythm's effects on neural HGP and MUA, we used Tort's MI (29) (Figs. 6*D* and 7*B* and *SI Appendix*, Fig. S10*B*) with a nonparametric trial shuffling procedure to assess significance (*SI Appendix, SI Methods*).

Traveling Waves. We utilized 4.54 ± 0.87 min (mean ± SD) of ECoG recordings made for clinical purposes. These arrays had 2-mm contact diameters and 1-cm intercontact spacing and were referenced to 1 to 4 inactive electrodes placed outside of the dura facing the skull. In Pts. E1, E3, and E4, patients were instructed to open and close their eyes with an audial cue at 15-s intervals using Presentation software (Neurobehavioral Systems). We only utilized activity during eye closure in these patients (except for *SI Appendix*, Fig. S4). In Pts. E2 and E5 (who didn't participate in the eye-closure task), we analyzed spontaneous activity during quiet wakefulness. We also analyzed 16.5 min of open-source ECoG recordings made from a macaque monkey during an eye-closure task. Eyes were closed via a sleep mask for 10 min, and the sleep mask was then removed for 10 min of data. The macaque was included in group statistics with other patients due to its high similarity with human activity (*SI Appendix*, Fig. S4). Further details concerning the macaque recording can be found at Neurotycho.org (21). Time-domain data in Pts. E1 and E5 were spatially interpolated in missing channels [using inpaint_nans (75)] prior to further analysis.

To localize contacts to the pial surface, we aligned a preoperative MRI with a structural MRI or computed tomography (CT). These contact locations were then displayed on the reconstructed cortical surface, created by using Freesurfer (76), of each individual patient (Figs. 1 and 2) (77, 78).

Traveling wave analyses were performed separately for the strip and grid ECoG arrays in the macaque, as well as the 2 strips in Pt. E1, as the large cortical distances between the electrodes would make phase differences difficult to interpret.

We then wished to measure the directionality of these traveling waves. To do this, we employed the phase-gradient ∇, found by using MATLAB's gradient function (but with subtractions replaced with circular distances). To prove that there was a consistent directionality of propagation across time, at each time point, we found the mean direction of the gradient throughout the grid. Using Rayleigh's test for nonuniformity demonstrated that each patient had a significant propagation direction (*SI Appendix*, Fig. S4). To generate Fig. 2*D*, we binned the traveling-wave directions across time into 100 bins normalized within patients (i.e., divided the count of each bin by the total number of time points) and then averaged across patients (with the error bar being the SEM across patients).

To find instantaneous speeds across time, the grid's instantaneous frequency first needed to be estimated. This was done by taking the first derivative of the instantaneous alpha phase over time (*SI Appendix, SI Methods*). Instantaneous speeds were then calculated as follows: Each channel's instantaneous frequency was divided by the magnitude of its phase gradient $\left(\sqrt{\nabla_x^2 + \nabla_y^2}\right)$, yielding the instantaneous speed at each channel and time point. Then, at each time point, the median speed and frequency across all channels was found, and time points with a speed or frequency in the top or bottom 0.5th percentile were rejected to eliminate outliers. The distribution of these median speeds across time was then plotted as a normalized histogram (bin width of 0.01 m/s) for each patient and presented in *SI Appendix*, Fig. S4. These normalized histograms were averaged and plotted in Fig. 2*C*.

To ensure that this effect was specific to the alpha band, we reapplied our main analysis to 2-Hz filtered bands with 1-Hz spacing from 1 to 35 Hz and found the resultant vector length of propagation direction across all time points. A clear alpha peak was observed (*SI Appendix*, Fig. S3).

Corticothalamic Interactions. SEEG (79) was performed on 9 patients to characterize epileptogenic activity and inform possible resections. SEEG macroelectrode depth probes had 10–15 contacts; each contact was 2 mm long and 0.8 mm in diameter with 1.5-mm intercontact spacing. The probes themselves were ~5 cm long, with the exact length varying between electrodes. In Pts. S1 to S7, contact locations were found by stereotactic teleradiographs

from within the stereotactic frame. These coordinates were then superimposed on a T1 MRI of the subject. An atlas (80) was then overlaid to determine the anatomical positions of thalamic and cortical contacts (Fig. 3*A*). Contacts were localized in Pts. S8 and S9 by aligning a postoperative CT with a preoperative MRI. Adjacent channels (when at least 1 was in the gray matter) were referenced to each other to assure local generation of measured activity. Further use of contact, channel, or site all refer to these bipolar channel pairs. Recordings were made at 256 Hz in Pts. S1 to S3, 128 Hz in Pts. S4 to S7, and 1,024 Hz in Pts. S8 and S9. For further details, see ref. 81.

We analyzed spontaneous activity (36 ± 7.5 min, mean ± SD) during wakefulness prior to the onset of sleep, the time of which was determined behaviorally as well as electrographically by a qualified sleep stager using standard methods (82). The last 3 min of wakefulness before the onset of sleep was rejected to further avoid the analysis of sleep or excess drowsiness.

Prior to further analyses, we split the data into nonoverlapping 2-s epochs. We bandpass filtered (2-pass 3rd-order Butterworth) thalamic activity in the alpha band, then found the absolute value of its analytic signal (hilbert.m) to find single-trial thalamic alpha amplitude. Then, the 20% of epochs with the most total alpha-band amplitude (summing across thalamic bipolar pairs and samples) were used for further processing.

Cortical and thalamic power spectral peaks were found by using the peakfinder (83) algorithm with a selectivity (the minimum difference a local maxima must have from the nearest local minima to be considered a peak) of the power spectrum's range divided by 5. A channel was considered to have an alpha peak if it had at least 1 peak between 7 and 13 Hz.

To phase-align ongoing alpha activity (Fig. 4*D*), we picked the thalamic contact with the greatest alpha-band power and averaged the rest of our data (cortical and thalamic wide-band LFP and HGP) to alpha-band peaks in this channel. Alpha-band peaks were found by bandpass filtering from 7 to 13 Hz (2-pass 3rd-order Butterworth), taking the angle of the analytic signal (hilbert.m) to find the phase, and then finding peaks in this series. LFP was high-pass filtered at 2 Hz (2-pass 3rd-order Butterworth) prior to averaging on alpha peaks.

HGP was derived by filtering from 70 to 120 Hz in Pts. S1 to S3 (due to a Nyquist frequency of 128 Hz) and 70 to 190 Hz in Pts. S8 and S9. The sampling rate in Pts. S4 to S7 (128 Hz) was too low to measure HGP. Although the former frequency band was somewhat lower than the usual definition of HGP (70 to 190 Hz), we observed similar results in patients with both usual and reduced HGP bands (*SI Appendix*, Fig. S10). Furthermore, a previous study employing the same recordings demonstrated that 70- to 120-Hz HGP reliably decreased during K-complexes identical to 70- to 190-Hz power (81). Lastly, reanalyzing Pts. S8 and S9 using the 70- to 120-Hz band yielded highly similar results. Seven of 14 (coherence) or 10 of 14 (MI) thalamic channels exhibited significant PAC between thalamic alpha LFPg and the HGP of at least 1 cortical channel (compare to 9 of 14 coherence and 10 of 14 MI with 70- to 190-Hz band). Furthermore, 0 of 14 (coherence) or 4 of 14 (MI) thalamic channels had significant PAC between thalamic alpha LFPg and thalamic HGP (0 of 14 [coherence] and 3 of 14 [MI] with the 70- to 190-Hz band).

The SR was measured as described in Cole et al. (31) (*SI Appendix*, *SI Methods*).

GC analyses were performed by using the Multivariate GC Toolbox (34). Frequency-resolved GC values were assessed between each corticothalamic channel pair in the nonoverlapping 2-s epochs with the greatest 20% of thalamic alpha amplitude (derived from the analytic signal computed with hilbert.m) (*SI Appendix*, *SI Methods*).

Laminar Recordings. Laminar microelectrodes were implanted perpendicular to the cortex in noneloquent tissue that was ultimately resected (35) (*SI Appendix*, *SI Methods*). Each laminar probe spanned the cortical depth with a length of 3.5 mm and diameter of 0.35 mm. Contacts had 40-μm diameters, spaced at 175 μm in Pt. L1 and 150 μm in Pts. L2 and L3. Recordings were made during 11.32 ± 0.48 min (mean ± SD) of quiet wakefulness.

The LFPg, or the first derivative of the field potential (i.e., each contact referenced to its neighbor) and MUA were recorded simultaneously at 2,000 and 20,000 Hz and filtered online from 0.2 to 500 Hz and 200 to 5,000 Hz, respectively. Data from faulty channels (2 in each patient) were linearly interpolated from the channels directly above and below them.

Line noise was eliminated from both the LFPg and MUA by band-stop filtering (4-Hz bandwidth) at 60 Hz in Pts. L1 and L2 and 50 Hz in Pt. L3 (4th-order Butterworth). The LFPg was then high-pass filtered at 0.5 Hz in Pts. L2 and L3 and 3.5 Hz in Pt. L1 due to a low-frequency vascular artifact (2-pass 2nd-order Butterworth), HGP from 70 to 190 Hz, and MUA from 300 to 3,000 Hz (4th-order Butterworth). MUA was then rectified and resampled at 2,000 Hz. The data were then subsampled into 2-s artifact-free epochs, and, consistent with ECoG and SEEG, the 20% of epochs with the most alpha-band CSD amplitude across all channels were utilized for further analysis. In Pt. L1, all artifact-free epochs (not just those with the most alpha amplitude) were used due to a relatively short recording session. We observed no significant modulation of HGP or MUA in Pt. L1, probably due to technical issues with the recording such as gliosis or faulty electrodes.

CSD was measured by taking the first spatial derivative of the LFPg (in effect, the second spatial derivative of the monopolar field potential) and then applying a 5-point Hamming filter (35, 36). The Vaknin approximation (adding pseudochannels of zeros to the LFPg above and below the array) was used to estimate the CSD on the second-most deep and superficial channels of the laminar probe (84).

We localized laminar contacts to cortical layers by performing histology on explanted tissue in Pts. L1 and L3 and identifying a putative layer IV sink in Pt. L2 (*SI Appendix*, Fig. S12).

Code Availability. Custom scripts are publically available on GitHub (https://github.com/mhalgren/AlphaGen).

Data Availability. The data underlying our figures are available on figshare (85). Macaque data are publicly available at http://neurotycho.org/data/20120813ktanesthesiaandsleepchibitoruyanagawa.

ACKNOWLEDGMENTS. We thank Erica Johnson, Nathan Meng, Richárd Fiáth, Qianli Xu, and Adam Niese for insightful comments, hypotheses, and technical support; and Project Tycho for making their macaque dataset publicly available. This study was supported by US Office of Naval Research Grant N00014-13-1-0672; NIH Grants R01-MH-099645, R01-EB-009282, R01-NS-062092, and K24-NS-088568; the Massachusetts General Hospital Executive Council on Research; Hungarian National Brain Research Program Grants KTIA_13_NAP-A-IV/1- 4,6 and 2017-1.2.1-NKP-2017-00002; European Union Grant FP7 600925 NeuroSeeker; and Hungarian Government Grants OTKA PD101754 and OTKA K119443.

1. H. Berger, Das elektrenkephalogramm des menschen. *Naturwissenschaften* **23**, 121–124 (1935).
2. J. Ito, A. R. Nikolaev, C. van Leeuwen, Spatial and temporal structure of phase synchronization of spontaneous alpha EEG activity. *Biol. Cybern.* **92**, 54–60 (2005).
3. A. von Stein, J. Sarnthein, Different frequencies for different scales of cortical integration: From local gamma to long range alpha/theta synchronization. *Int. J. Psychophysiol.* **38**, 301–313 (2000).
4. Y. B. Saalmann, M. A. Pinsk, L. Wang, X. Li, S. Kastner, The pulvinar regulates information transmission between cortical areas based on attention demands. *Science* **337**, 753–756 (2012).
5. J. Samaha, B. R. Postle, The speed of alpha-band oscillations predicts the temporal resolution of visual perception. *Curr. Biol.* **25**, 2985–2990 (2015).
6. N. A. Busch, J. Dubois, R. VanRullen, The phase of ongoing EEG oscillations predicts visual perception. *J. Neurosci.* **29**, 7869–7876 (2009).
7. O. Jensen, A. Mazaheri, Shaping functional architecture by oscillatory alpha activity: Gating by inhibition. *Front. Hum. Neurosci.* **4**, 186 (2010).
8. E. J. Peterson, B. Voytek, Alpha oscillations control cortical gain by modulating excitatory- inhibitory background activity. bioRxiv:10.1101/185074 (7 September 2017).
9. O. Jensen, J. Gelfand, J. Kounios, J. E. Lisman, Oscillations in the alpha band (9-12 Hz) increase with memory load during retention in a short-term memory task. *Cereb. Cortex* **12**, 877–882 (2002).
10. M. L. Lorincz, K. A. Kékesi, G. Juhász, V. Crunelli, S. W. Hughes, Temporal framing of thalamic relay-mode firing by phasic inhibition during the alpha rhythm. *Neuron* **63**, 683–696 (2009).
11. S. W. Hughes *et al*., Thalamic gap junctions control local neuronal synchrony and influence macroscopic oscillation amplitude during EEG alpha rhythms. *Front. Psychol.* **2**, 193 (2011).
12. S. Vijayan, N. J. Kopell, Thalamic model of awake alpha oscillations and implications for stimulus processing. *Proc. Natl. Acad. Sci. U.S.A.* **109**, 18553–18558 (2012).
13. T. van Kerkoerle *et al*., Alpha and gamma oscillations characterize feedback and feedforward processing in monkey visual cortex. *Proc. Natl. Acad. Sci. U.S.A.* **111**, 14332–14341 (2014).
14. L. Silva, Y. Amitai, B. Connors, Intrinsic oscillations of neocortex generated by layer 5 pyramidal neurons. *Science* **251**, 432–435 (1991).
15. E. A. Buffalo, P. Fries, R. Landman, T. J. Buschman, R. Desimone, Laminar differences in gamma and alpha coherence in the ventral stream. *Proc. Natl. Acad. Sci. U.S.A.* **108**, 11262–11267 (2011).
16. J. F. Mejias, J. D. Murray, H. Kennedy, X.-J. Wang, Feedforward and feedback frequency-dependent interactions in a large-scale laminar network of the primate cortex. *Sci. Adv.* **2**, e1601335 (2016).
17. T. Womelsdorf, T. A. Valiante, N. T. Sahin, K. J. Miller, P. Tiesinga, Dynamic circuit motifs underlying rhythmic gain control, gating and integration. *Nat. Neurosci.* **17**, 1031–1039 (2014).

18. F. Roux, M. Wibral, W. Singer, J. Aru, P. J. Uhlhaas, The phase of thalamic alpha activity modulates cortical gamma-band activity: Evidence from resting-state MEG recordings. *J. Neurosci.* **33**, 17827–17835 (2013).
19. H. Zhang, J. Jacobs, Traveling theta waves in the human hippocampus. *J. Neurosci.* **35**, 12477–12487 (2015).
20. D. Rubino, K. A. Robbins, N. G. Hatsopoulos, Propagating waves mediate information transfer in the motor cortex. *Nat. Neurosci.* **9**, 1549–1557 (2006).
21. Y. Nagasaka, K. Shimoda, N. Fujii, Multidimensional recording (MDR) and data sharing: An ecological open research and educational platform for neuroscience. *PLoS One* **6**, e22561 (2011).
22. J.-Y. Moon *et al*., Structure shapes dynamics and directionality in diverse brain networks: Mathematical principles and empirical confirmation in three species. *Sci. Rep.* **7**, 46606 (2017).
23. R. Nieuwenhuys, J. Voogd, C. van Huijzen, *The Human Central Nervous System* (Springer, Berlin, 2008).
24. H. Zhou, R. J. Schafer, R. Desimone, Pulvinar-cortex interactions in vision and attention. *Neuron* **89**, 209–220 (2016).
25. R. A. Mak-McCully *et al*., Coordination of cortical and thalamic activity during non-REM sleep in humans. *Nat. Commun.* **8**, 15499 (2017).
26. G. B. Ermentrout, N. Kopell, Frequency plateaus in a chain of weakly coupled oscillators, I. *SIAM J. Math. Anal.* **15**, 215–237 (1984).
27. S. Vijayan, K. Q. Lepage, N. J. Kopell, S. S. Cash, Frontal beta-theta network during REM sleep. *eLife* **6**, e18894 (2017).
28. B. Nandi, P. Swiatek, B. Kocsis, M. Ding, Inferring the direction of rhythmic neural transmission via inter-regional phase-amplitude coupling (ir-PAC). *Sci. Rep.* **9**, 6933 (2019).
29. A. B. L. Tort, R. Komorowski, H. Eichenbaum, N. Kopell, Measuring phase-amplitude coupling between neuronal oscillations of different frequencies. *J. Neurophysiol.* **104**, 1195–1210 (2010).
30. L. L. Colgin *et al*., Frequency of gamma oscillations routes flow of information in the hippocampus. *Nature* **462**, 353–357 (2009).
31. S. R. Cole *et al*., Nonsinusoidal beta oscillations reflect cortical pathophysiology in Parkinson's disease. *J. Neurosci.* **37**, 4830–4840 (2017).
32. C. M. Sweeney-Reed *et al*., Anterior thalamic high frequency band activity is coupled with theta oscillations at rest. *Front. Hum. Neurosci.* **11**, 358 (2017).
33. E. L. Rich, J. D. Wallis, Spatiotemporal dynamics of information encoding revealed in orbitofrontal high-gamma. *Nat. Commun.* **8**, 1139 (2017).
34. L. Barnett, A. K. Seth, The MVGC multivariate Granger causality toolbox: A new approach to Granger-causal inference. *J. Neurosci. Methods* **223**, 50–68 (2014).
35. I. Ulbert, E. Halgren, G. Heit, G. Karmos, Multiple microelectrode-recording system for human intracortical applications. *J. Neurosci. Methods* **106**, 69–79 (2001).
36. C. Nicholson, J. A. Freeman, Theory of current source-density analysis and determination of conductivity tensor for anuran cerebellum. *J. Neurophysiol.* **38**, 356–368 (1975).
37. Y. Kajikawa, C. E. Schroeder, How local is the local field potential? *Neuron* **72**, 847–858 (2011).
38. G. Buzsáki, C. A. Anastassiou, C. Koch, The origin of extracellular fields and currents—EEG, ECoG, LFP and spikes. *Nat. Rev. Neurosci.* **13**, 407–420 (2012).
39. S. Haegens *et al*., Laminar profile and physiology of the α rhythm in primary visual, auditory, and somatosensory regions of neocortex. *J. Neurosci.* **35**, 14341–14352 (2015).
40. A. Bollimunta, J. Mo, C. E. Schroeder, M. Ding, Neuronal mechanisms and attentional modulation of corticothalamic α oscillations. *J. Neurosci.* **31**, 4935–4943 (2011).
41. A. Bollimunta, Y. Chen, C. E. Schroeder, M. Ding, Neuronal mechanisms of cortical alpha oscillations in awake-behaving macaques. *J. Neurosci.* **28**, 9976–9988 (2008).
42. M. Leszczynski *et al*., Dissociation of broadband high-frequency activity and neuronal firing in the neocortex. bioRxiv:10.1101/531368 (25 January 2019).
43. A. Bahramisharif *et al*., Propagating neocortical gamma bursts are coordinated by traveling alpha waves. *J. Neurosci.* **33**, 18849–18854 (2013).
44. L. E. Martinet *et al*., Human seizures couple across spatial scales through travelling wave dynamics. *Nat. Commun.* **8**, 14896 (2017).
45. S. Arroyo *et al*., Functional significance of the mu rhythm of human cortex: An electrophysiologic study with subdural electrodes. *Electroencephalogr. Clin. Neurophysiol.* **87**, 76–87 (1993).
46. Y. Iwamura, Hierarchical somatosensory processing. *Curr. Opin. Neurobiol.* **8**, 522–528 (1998).
47. H. C. Dijkerman, E. H. F. de Haan, Somatosensory processes subserving perception and action. *Behav. Brain Sci.* **30**, 189–201, discussion 201–239 (2007).
48. K. Inui, X. Wang, Y. Tamura, Y. Kaneoke, R. Kakigi, Serial processing in the human somatosensory system. *Cereb. Cortex* **14**, 851–857 (2004).
49. D. Lozano-Soldevilla, R. VanRullen, The hidden spatial dimension of alpha: 10-Hz perceptual echoes propagate as periodic traveling waves in the human brain. *Cell Rep.* **26**, 374–380.e4 (2019).
50. A. Alamia, R. Vanrullen, Alpha oscillations and travelling waves: Signatures of predictive coding? bioRxiv:10.1101/464933 (7 November 2018).
51. H. Zhang, A. J. Watrous, A. Patel, J. Jacobs, Theta and alpha oscillations are traveling waves in the human neocortex. *Neuron* **98**, 1269–1281.e4 (2018).
52. G. B. Ermentrout, D. Kleinfeld, Traveling electrical waves in cortex: Insights from phase dynamics and speculation on a computational role. *Neuron* **29**, 33–44 (2001).
53. F. Han, N. Caporale, Y. Dan, Reverberation of recent visual experience in spontaneous cortical waves. *Neuron* **60**, 321–327 (2008).
54. V. Crunelli *et al*., Dual function of thalamic low-vigilance state oscillations: Rhythm-regulation and plasticity. *Nat. Rev. Neurosci.* **19**, 107–118 (2018).
55. F. H. da Silva, T. H. M. T. van Lierop, C. F. Schrijer, W. S. van Leeuwen, Organization of thalamic and cortical alpha rhythms: Spectra and coherences. *Electroencephalogr. Clin. Neurophysiol.* **35**, 627–639 (1973).
56. S. W. Hughes, V. Crunelli, Thalamic mechanisms of EEG alpha rhythms and their pathological implications. *Neuroscientist* **11**, 357–372 (2005).
57. I. C. Fiebelkorn, M. A. Pinsk, S. Kastner, The mediodorsal pulvinar coordinates the macaque fronto-parietal network during rhythmic spatial attention. *Nat. Commun.* **10**, 215 (2019).
58. S. Quax, O. Jensen, P. Tiesinga, Top-down control of cortical gamma-band communication via pulvinar induced phase shifts in the alpha rhythm. *PLoS Comput. Biol.* **13**, e1005519 (2017).
59. E. G. Jones, Thalamic circuitry and thalamocortical synchrony. *Philos. Trans. R. Soc. Lond. B Biol. Sci.* **357**, 1659–1673 (2002).
60. V. Zotev, M. Misaki, R. Phillips, C. K. Wong, J. Bodurka, Real-time fMRI neurofeedback of the mediodorsal and anterior thalamus enhances correlation between thalamic BOLD activity and alpha EEG rhythm. *Hum. Brain Mapp.* **39**, 1024–1042 (2018).
61. S. R. Crandall, S. J. Cruikshank, B. W. Connors, A corticothalamic switch: Controlling the thalamus with dynamic synapses. *Neuron* **86**, 768–782 (2015).
62. N. T. Markov *et al*., Anatomy of hierarchy: Feedforward and feedback pathways in macaque visual cortex. *J. Comp. Neurol.* **522**, 225–259 (2014).
63. P. Girard, J. M. Hupé, J. Bullier, Feedforward and feedback connections between areas V1 and V2 of the monkey have similar rapid conduction velocities. *J. Neurophysiol.* **85**, 1328–1331 (2001).
64. A. M. Bastos, R. Loonis, S. Kornblith, M. Lundqvist, E. K. Miller, Laminar recordings in frontal cortex suggest distinct layers for maintenance and control of working memory. *Proc. Natl. Acad. Sci. U.S.A.* **115**, 1117–1122 (2018).
65. R. Csercsa *et al*., Laminar analysis of slow wave activity in humans. *Brain* **133**, 2814–2829 (2010).
66. E. Halgren *et al*., Laminar profile of spontaneous and evoked theta: Rhythmic modulation of cortical processing during word integration. *Neuropsychologia* **76**, 108–124 (2015).
67. M. Halgren *et al*., Superficial slow rhythms integrate cortical processing in humans. *Sci. Rep.* **8**, 2055 (2018).
68. S. Haegens, V. Nácher, R. Luna, R. Romo, O. Jensen, α-Oscillations in the monkey sensorimotor network influence discrimination performance by rhythmical inhibition of neuronal spiking. *Proc. Natl. Acad. Sci. U.S.A.* **108**, 19377–19382 (2011).
69. A. J. Billig *et al*., A sound-sensitive source of alpha oscillations in human non-primary auditory cortex. *J. Neurosci.*, 0696-19 (2019).
70. M. Larkum, A cellular mechanism for cortical associations: An organizing principle for the cerebral cortex. *Trends Neurosci.* **36**, 141–151 (2013).
71. H. S. Meyer *et al*., Inhibitory interneurons in a cortical column form hot zones of inhibition in layers 2 and 5A. *Proc. Natl. Acad. Sci. U.S.A.* **108**, 16807–16812 (2011).
72. P. Berens, CircStat: A MATLAB toolbox for circular statistics. *J. Stat. Softw.* **31**, 1–21 (2009).
73. R. Oostenveld, P. Fries, E. Maris, J.-M. Schoffelen, FieldTrip: Open source software for advanced analysis of MEG, EEG, and invasive electrophysiological data. *Comput. Intell. Neurosci.* **2011**, 156869 (2011).
74. J. R. Rosenberg, A. M. Amjad, P. Breeze, D. R. Brillinger, D. M. Halliday, The Fourier approach to the identification of functional coupling between neuronal spike trains. *Prog. Biophys. Mol. Biol.* **53**, 1–31 (1989).
75. J. D'Errico, inpaint_nans, Version 1.1.0.0. https://www.mathworks.com/matlabcentral/fileexchange/4551-inpaint_nans. Accessed 3 July 2017.
76. A. M. Dale, B. Fischl, M. I. Sereno, Cortical surface-based analysis. I. Segmentation and surface reconstruction. *Neuroimage* **9**, 179–194 (1999).
77. A. I. Yang *et al*., Localization of dense intracranial electrode arrays using magnetic resonance imaging. *Neuroimage* **63**, 157–165 (2012).
78. A. R. Dykstra *et al*., Individualized localization and cortical surface-based registration of intracranial electrodes. *Neuroimage* **59**, 3563–3570 (2012).
79. J. Talairach *et al*., Surgical therapy for frontal epilepsies. *Adv. Neurol.* **57**, 707–732 (1992).
80. A. Morel, M. Magnin, D. Jeanmonod, Multiarchitectonic and stereotactic atlas of the human thalamus. *J. Comp. Neurol.* **387**, 588–630 (1997).
81. R. A. Mak-McCully *et al*., Distribution, amplitude, incidence, co-occurrence, and propagation of human K-complexes in focal transcortical recordings. *eNeuro* **2**, ENEURO.0028-15.2015 (2015).
82. A. Rechtschaffen, A. Kales, A manual of standardised terminology, techniques, and scoring system for sleep stages of human subjects. *Los Angelos UCLA Brain Inf. Serv.* **02115**, 2115 (1968).
83. N. Yoder, Peakfinder. https://www.mathworks.com/matlabcentral/answers/uploaded_files/23997/peakfinder.m. Accessed 5 February 2017.
84. G. Vaknin, P. G. DiScenna, T. J. Teyler, A method for calculating current source density (CSD) analysis without resorting to recording sites outside the sampling volume. *J. Neurosci. Methods* **24**, 131–135 (1988).
85. M. Halgren *et al*., Alpha figures dataset. Figshare. 10.6084/m9.figshare.9927125.v2. Deposited 2 October 2019.
86. I. Ulbert, G. Karmos, G. Heit, E. Halgren, Early discrimination of coherent versus incoherent motion by multiunit and synaptic activity in human putative MT+. *Hum. Brain Mapp.* **13**, 226–238 (2001).
87. C. Teufel, S. C. Dakin, P. C. Fletcher, Prior object-knowledge sharpens properties of early visual feature-detectors. *Sci. Rep.* **8**, 10853 (2018).